

Analysis of intermediary scan-lens and tube-lens mechanisms for optical coherence tomography

FARID ATRY AND RAMIN PASHAIE*

Electrical Engineering and Computer Sciences Department, University of Wisconsin-Milwaukee, 3200 North Cramer Street, Milwaukee, Wisconsin 53211, USA

*Corresponding author: pashaie@uwm.edu

Received 13 October 2015; revised 3 December 2015; accepted 14 December 2015; posted 15 December 2015 (Doc. ID 251873); published 21 January 2016

Combining an optical coherence tomography (OCT) scanner with other techniques such as optogenetic neurostimulation or fluorescence imaging requires integrating auxiliary components into the optical path of the setup. Due to the short scanning distance of most OCT objectives, adding scan and tube lenses in the device is essential to open space between the back-focal-plane of the objective and center of mass of the mirrors in the galvanometer. The effect of the scan and tube lenses on the focal spot size of the scanner using off-the-shelf components are theoretically explored for three different designs in this paper. Two lens mechanisms were implemented and tested in a custom-built OCT scanner to experimentally measure point-spread functions. Based on our analysis, proper form of a four-element semi-Plössl lens provides a superior performance compared with an achromatic doublet when used as a scan/tube lens. The former lens design provides close to diffraction-limited resolution for scan angles up to 6.4° ; however, due to aberrations in an achromatic doublet, the later design offers diffraction-limited resolution confined to 2° scan angles. © 2016 Optical Society of America

OCIS codes: (110.4500) Optical coherence tomography; (180.0180) Microscopy; (180.1790) Confocal microscopy; (220.3620) Lens system design.

<http://dx.doi.org/10.1364/AO.55.000646>

1. INTRODUCTION

Since its introduction in 1991 [1], optical coherence tomography (OCT) has been widely used to obtain 3D images of semi-transparent specimens [2–13]. OCT is a nondestructive imaging modality in which a sample is illuminated by a low-coherence light beam. Photons that backscatter from different depths in the sample are separated by employing low-coherence interferometry techniques. The axial resolution of this imaging modality is determined by the coherence length of the source, and it can achieve micron-scale resolution up to a few millimeters deep inside a sample [2]. For large spectral bandwidth-light sources, the axial resolution can be close to $1\ \mu\text{m}$ [14–19], which is significantly smaller than the imaging resolution of some other imaging modalities such as computed tomography (CT) and magnetic resonance imaging (MRI) systems.

The lateral resolution in an OCT scanner is independent of its axial resolution and hinges mostly on the lensing system of the device. Specific objective lenses are introduced for laser-scanning microscopy to obtain diffraction-limited resolution over a large field-of-view (FOV), which is essential for most OCT applications. By placing a set of rotatory galvanometric mirrors at the back-focal-plane (BFP) of an OCT objective, a

specimen is scanned over the transverse plane (x and y directions). The block diagram of a typical spectral-domain OCT system is depicted in Fig. 1. Since the galvanometer has two mirrors, the best performance is achieved when the BFP of the objective is equidistant from both mirrors. The same alignment is used in conventional time-domain and swept-source OCT systems.

OCT, in combination with other optical platforms such as multiphoton microscopy [20–22] or optical neurostimulation [23], enables researchers to access some details of functional activities that were not available before. To separate beam paths of different modalities, intermediary optical components, e.g., dichroic mirrors, are needed between the objective lens and the galvanometric mirrors. However, the short BFP distance for most OCT objective lenses is a limiting factor and a lens system consisting of a scan lens and a tube lens is required to open the necessary space for the auxiliary optics. Figure 2 demonstrates a scan-/tube-lens mechanism placed before an objective lens so that a dichroic mirror can be integrated in the optical path. Imperfections in the lens system introduce optical aberrations, which affect the OCT resolution. Chromatic aberrations (longitudinal and lateral) in a lens prevent different wavelengths from focusing at the same focal point. Equally important,

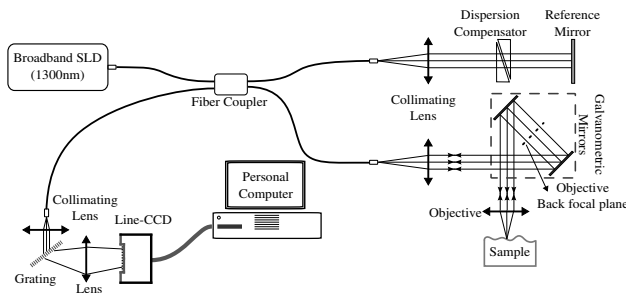


Fig. 1. Schematic of a typical spectral-domain OCT system. A set of galvanometric mirrors is used to scan a sample. The mirrors need to be located such that the BFP of an objective lens is at equal distances from both mirrors. For objectives with large numerical aperture, the distance between the lens barrel and BFP is not sufficient to place the galvanometric mirrors at the designated position or integrate intermediary optical components such as a dichroic mirror within the space between the objective and the scanning mirrors.

astigmatism causes sagittal and tangential light rays to focus at different axial positions. These imperfections increase the focal-spot size of the lens system and therefore degrade the resolution of an OCT scanner. Moreover, in the presence of a large Petzval field curvature (PFC), the focal plane is not flat and OCT images do not have a uniform resolution across the transversal surface.

The majority of OCT systems utilize infrared light (central wavelength around 1300 nm) to achieve sufficient penetration depth inside a scattering medium such as brain tissue. Also, it is desirable to have a FOV of a few millimeters with a lateral resolution in the range of 3.6–10 μm in most OCT applications. Achieving micron resolution in the infrared spectrum requires the optical system to perform close to its diffraction limit. Aberrations in the intermediary optics worsen the resolution and degrade the quality of OCT images.

Negrean and Mansvelder [24] have investigated the effects of scan-/tube-lens mechanisms on the performance of two-photon laser-scanning microscopes and proposed customized lens designs to achieve diffraction-limited resolution over a large FOV. A similar study on the performance of different

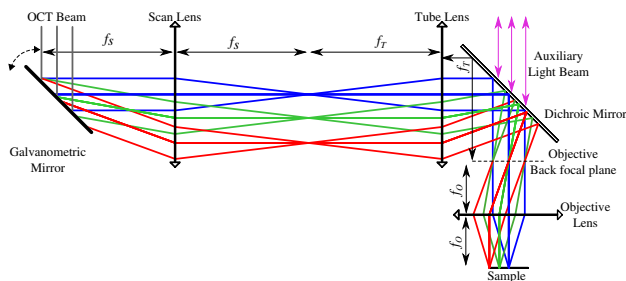


Fig. 2. Schematic of a scan lens and a tube lens in an OCT optical path. A galvanometric mirror is located at the focal of the scan lens and the scan-/tube-lens mechanism projects the OCT beam on the BFP of the objective lens. A dichroic mirror is added to separate the OCT beam and an auxiliary beam. An auxiliary light beam can be used for other imaging modalities or optogenetic stimulation applications. f_s , f_T , and f_O are, respectively, the focal lengths of the scan lens, tube lens, and objective.

scan-/tube-lens mechanisms for OCT applications seemed necessary. In this paper we analyze the effect of different designs of a scan lens and tube lens on the lateral resolution of an OCT device. First we used Zemax optical-design software to compare the performance of three popular and inexpensive lens systems, which are based on off-the-shelf components, as a scan/tube lens. Then, we constructed two of these lens mechanisms and used them in a custom-built OCT system to quantify their effect on the point-spread function (PSF) of the device. The practical PSF was measured using a 3D phantom with embedded sub-resolution gold nanoshells. Our results demonstrate that using single lenses as scan and tube lenses confines the area with diffraction-limited resolution to the central part of FOV, which is twice as large when using four-element Plössl type scan and tube lenses. This limitation of single-lens mechanisms is mostly due to large astigmatism and PFC in these lenses.

2. OPTICAL SIMULATIONS

For our fiber-based OCT system we considered a PSF with a full-width at half-maximum (FWHM) of $\sim 5 \mu\text{m}$, which is within the resolution range of typical OCT scanners [25–29]. In practice, we used an OCT objective lens with an effective focal length of 18 mm (LSM02, Thorlabs, New Jersey, USA) in combination with a collimator lens that provides a beam waist of 3.4 mm $\varnothing \frac{1}{e^2}$ at 1310 nm (F280APC-C, Thorlabs, New Jersey, USA). According to the Gaussian beam propagation equation [30], the FWHM focal-spot size of this combination is $\sim 5.16 \mu\text{m}$, which is close to the desired resolution. Simulation parameters were selected according to the practical setup, and a paraxial-lens model of focal length 18 mm was used as an objective lens. With this lens a scan angle of $\pm 6.4^\circ$ results in a scan-field radius of 2 mm. Moreover, in the design process a reciprocal structure with a $1\times$ magnification was considered for the intermediate lens system. In our OCT the collimating lens and objective have similar effective focal lengths and no magnification is required to achieve the desired resolution. Since the illumination and backscattered light travel via the same lens mechanism in a two-way path, a similar performance in both directions serves the purpose of this design.

A. Scan-Lens and Tube-Lens Simulations

Three common lens designs for scan/tube lenses were analyzed and their effects on the focal-spot size were investigated. The first two lens systems consist of single lenses and the third lens system uses a four element-lens mechanism (similar to Plössl compound) for a scan lens and tube lens. The same lens structure was used for both a scan lens and tube lens to achieve reciprocal performance.

1. Biconvex Singlet Lenses

The simplest relay lens system would be two lenses that are placed in a $4f$ configuration. Since OCT light sources are wideband (typical bandwidth of $\sim 100 \text{ nm}$ or larger) it is necessary to use lenses that are properly designed for such a wide spectrum. Calcium fluoride (CaF_2) has low dispersion in the near infrared spectrum. Consequently, lenses that are made from CaF_2 generally introduce low chromatic aberration over

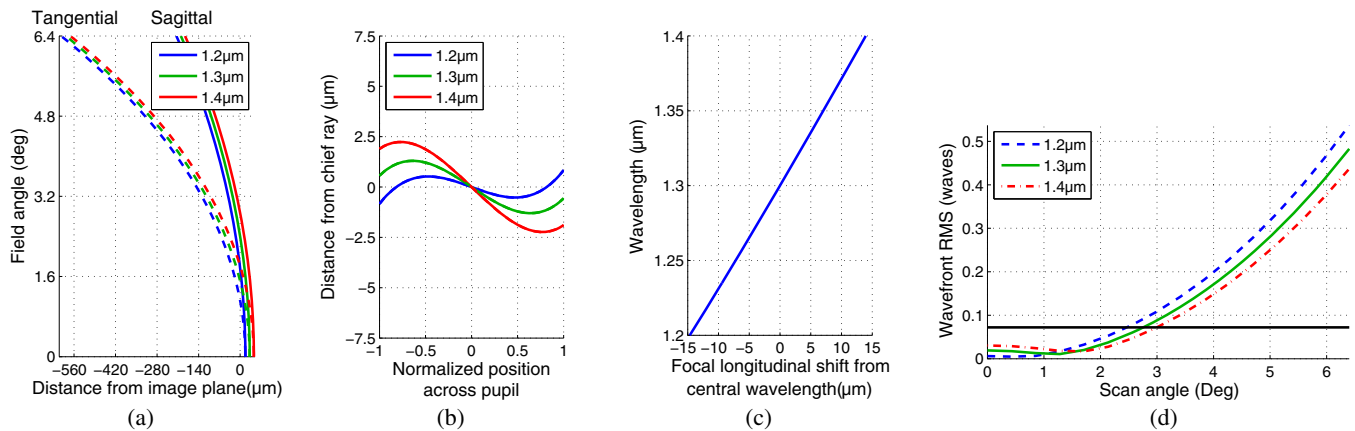


Fig. 3. Optical aberrations when two CaF2 lenses (LB5284, Thorlabs, New Jersey, USA) are used as scan and tube lenses in combination with an 18 mm focal-length objective lens. (a) Field curvature and astigmatic aberrations, (b) ray aberration as a function of pupil coordinate, (c) chromatic focal shift, and (d) wavefront RMS versus scan angle.

a wide bandwidth at the center wavelength of 1300 nm. In our first design we used biconvex CaF2 lenses of focal length 50 mm (LB5284, Thorlabs, New Jersey, USA) as the scan/tube lens. Simulations show a severe astigmatic aberration for this lens, which can degrade the performance of an OCT system. When the corresponding $4f$ lens system is used with the paraxial objective model at the maximum scan angle (6.4°), sagittal and tangential rays come to focus around 200 and 590 μm away from the focal plane, respectively, because of the field curvature and astigmatism aberrations. The separation between the focal of sagittal and tangential rays (>380 μm) at this scan angle is significantly larger than the Rayleigh range of the light beam (~ 46 μm) and worsens the OCT resolution at the corners of the FOV. This can be confirmed by the root mean square (RMS) of the wavefront error, which exceeds the diffraction limit threshold (0.072 waves) at scan angles larger than 2.7° . Consequently, with this lens mechanism the diffraction-limited FOV is confined to an area with a diameter smaller than 1.7 mm (Fig. 3).

2. Achromatic Doublet

Achromatic doublets (AD) are designed to introduce less spherical and chromatic aberrations to an optical beam compared to singlet lenses. Therefore, the next lens we studied was an AD of focal length ~ 50 mm (AC254-050-C, Thorlabs, New Jersey, USA). With this lens we observed smaller spherical aberration than the previous lens at a similar chromatic aberration (Fig. 4). Since these aberrations are already below the diffraction limit of our system, this improvement does not provide any superiority over the CaF2 lens. However, the AD lens introduces larger astigmatic and field curvature aberrations to the light beam compared with the CaF2 lens, which further reduces the diffraction-limited FOV compared with the previous lens system. As presented in Fig. 4(d), when two AC254-050-Cs are employed as the scan lens and tube lens, the RMS wavefront error increases above the diffraction limit at scan angles $>1.9^\circ$ and the diffraction-limited resolution is confined to a FOV of radius ~ 1.2 mm. At the scan angle of 6.4° , the separation between tangential and sagittal

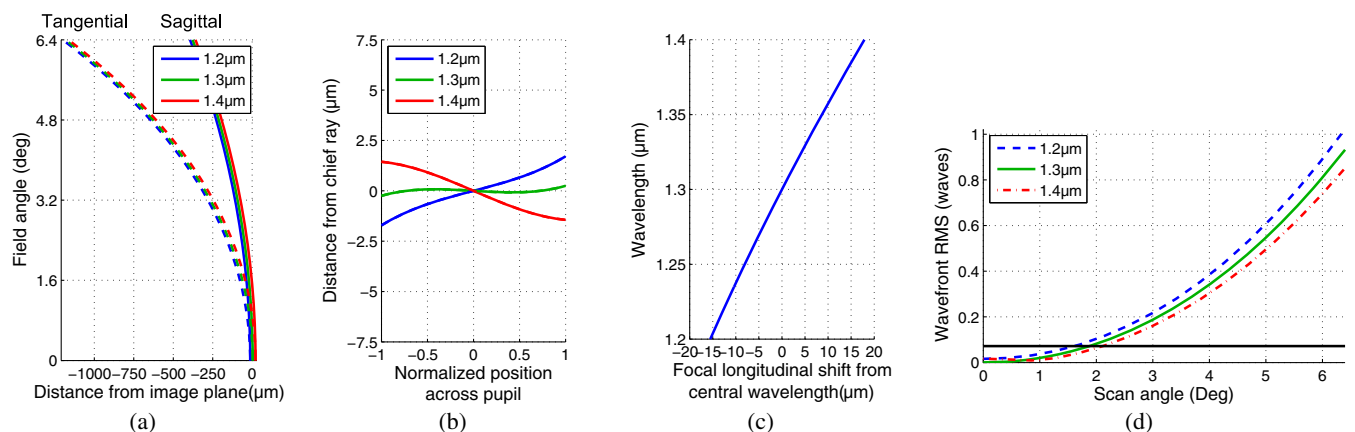


Fig. 4. Optical aberrations when two achromatic doublet lenses (AC254-050-C, Thorlabs, New Jersey, USA) are used as scan and tube lenses in combination with a paraxial objective with an 18 mm focal-length objective lens. (a) Field curvature and astigmatic aberrations, (b) ray aberration as a function of pupil coordinate, (c) chromatic focal shift, and (d) wavefront RMS versus scan angle.

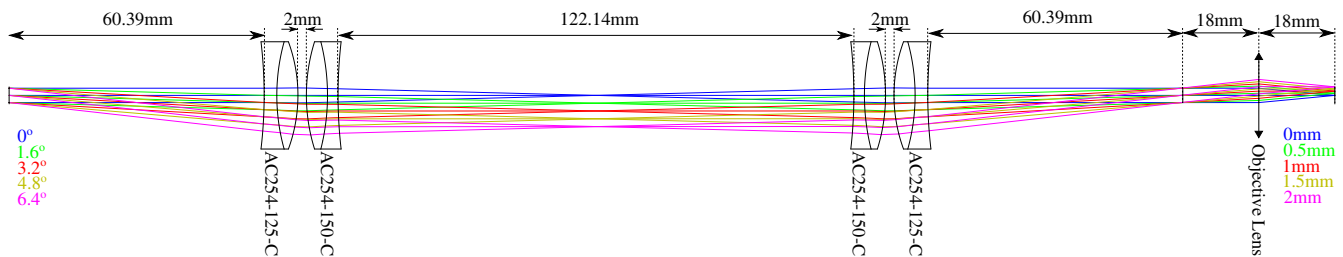


Fig. 5. Schematic of the lens mechanism based on four-element scan/tube lens. The effective focal length of the lens compound is ~ 66 mm.

focal planes is more than $800 \mu\text{m}$. The focal-spot size enlargement due to the severe astigmatism considerably reduces the signal to noise ratio of OCT images at large scan angles as well. Several lens providers offer various designs for AD lenses with different performance levels. Although some of the designs show moderately improved astigmatism, all models available on-line introduce a large amount of astigmatism to the light beam. This paper presents our data for AC254-050-C and compares its performance to a more advanced lens system.

3. Four-Element Semi-Plössl Compound

A Plössl compound lens is usually used as an eyepiece, and according to its good performance we considered it as a potential scan/tube lens. Generally, a Plössl compound lens consists of two identical achromatic doublets; however, by removing this constraint we were able to test a more diverse collection of lenses. To make an asymmetric semi-Plössl compound of the desired focal length (between 50 and 85 mm), we used two achromatic doublets with focal lengths of ~ 125 mm (AC254-125-C, Thorlabs, New Jersey, USA) and ~ 150 mm (AC254-150-C, Thorlabs, New Jersey, USA) (Fig. 5). The lens compound has an effective focal length of ~ 66 mm, and its performance is summarized in Fig. 6. This simple lens system introduces a fairly small amount of aberrations and performs close to the diffraction limit at field angles smaller than 6.4° (FOV of radius 4 mm combined with the designated objective).

The field curvature and astigmatic aberrations, which were the major limiting factors in the previous lens mechanisms, are significantly reduced when using this semi-Plössl compound. At the maximum scan angle, Petzval field curvature is $\sim 13 \mu\text{m}$ toward the lens for sagittal rays and $\sim 44 \mu\text{m}$ away from the lens for tangential rays. The curvature is negligible for many applications. Also the separation between sagittal and tangential focal planes is $58 \mu\text{m}$, which is marginally larger than the Rayleigh length. However, the RMS wavefront error at this scan angle is smaller than the diffraction-limit threshold, and the overall lens system performs within the diffraction limit over a FOV of radius 2 mm.

B. Aberrations in the Objective Lens

To measure performance of each relay lens in practice, we used an objective lens that is designed for OCT applications (LSM02, Thorlabs, New Jersey, USA). With an incident beam waist of $3.4 \text{ mm } \varnothing_{\frac{1}{e^2}}$ at a wavelength of 1300 nm , the theoretical FWHM of its focal spot is $5.16 \mu\text{m}$ and the corresponding Rayleigh range is $\sim 46 \mu\text{m}$. Using the Zemax black-box model provided by the manufacturer we estimated the amount of different aberrations introduced by the LSM02 objective, and the results are illustrated in Fig. 7. In these simulations the maximum scan angle was set to 6.4° , which translates to a 4 mm diameter FOV. The aberrations associated with this objective are negligible and do not degrade the resolution of the OCT system.

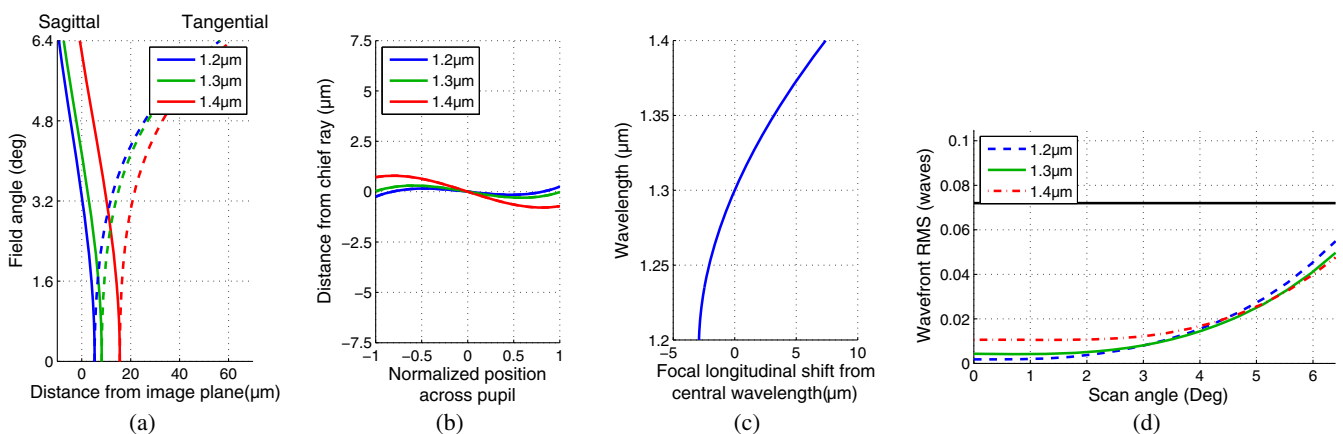


Fig. 6. Optical aberrations when two semi-Plössl compound lenses (AC254-125-C+AC254-150-C, Thorlabs, New Jersey, USA) are used as scan and tube lenses in combination with an 18 mm focal-length objective lens. (a) Field curvature and astigmatic aberrations, (b) ray aberration as a function of pupil coordinate, (c) chromatic focal shift, and (d) wavefront RMS versus scan angle.

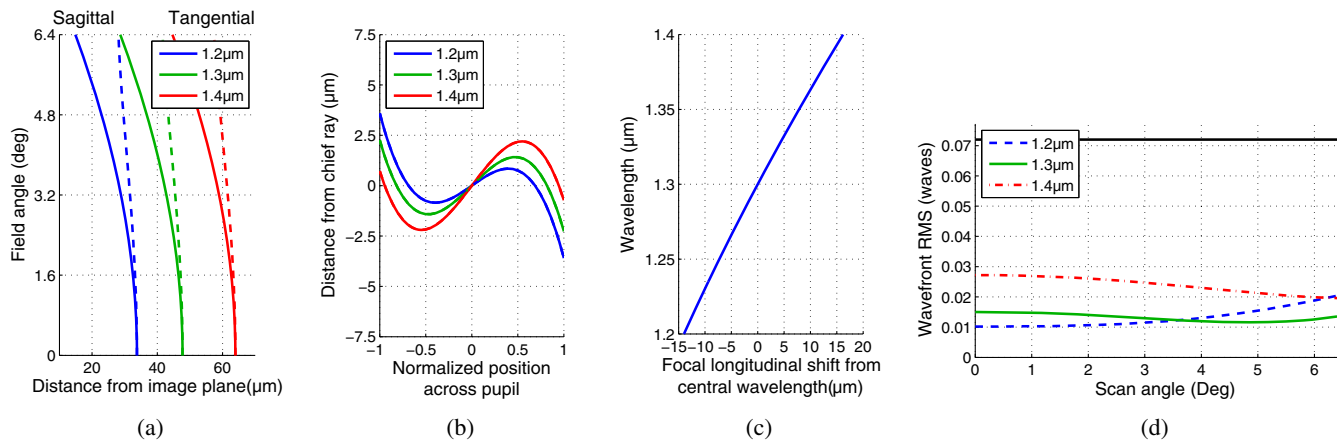


Fig. 7. Ray-tracing simulation using Zemax for LSM02 OCT objective lens. (a) Field curvature and astigmatic aberrations, (b) ray aberration as a function of pupil coordinate, (c) chromatic focal shift, and (d) wavefront RMS versus scan angle.

3. EXPERIMENTAL RESULTS

Two different scan-/tube-lens mechanisms were assembled using achromatic doublets or semi-Plössl lenses, and the PSFs of the corresponding OCT systems were obtained. The FWHM values of the PSFs are reported as a resolution for the OCT system to compare the performance of different relay-lens mechanisms. A 3D phantom with embedded gold nano-shells was produced to measure the PSF as described in the following section.

A. Sample Preparation

In recent years several groups have attempted to measure the PSF of OCT systems [31–34] by fabricating 3D phantoms with embedded sub-resolution particles. We prepared a 3D sample following a procedure similar to what was described in [31]. To make our sample we desiccated a 130 μL suspension of gold nano-shells. The nano-shells consist of a silica core of radius ~ 99 nm and a gold shell of $16.4 \text{ nm} \pm 5.9$ nm thickness (980 nm Resonant Gold Nanoshells, nanoComposix, California, USA). Then nano-shells were dispersed in 20 mL of epoxy resin (EpoxyCure Epoxy Resin, 20-8130-128, Buehler, Illinois, USA) using an ultrasonic bath. At the end, 5 mL of an epoxy hardener (EpoxyCure Epoxy Hardener, 20-8132-032, Buehler, Illinois, USA) was slowly added and mixed with the resin mixture and allowed to harden for approximately 12 h. The spacing between the gold nano-shells was estimated to be $\sim 50 \mu\text{m}$. Since the particles were selected to be significantly smaller than the theoretical PSF of our imaging system ($0.22 \mu\text{m}$ compared to $5.16 \mu\text{m}$), the image formed by each particle is representing the PSF of our imaging system.

B. OCT System

The lens mechanisms were used in a custom-built fiber-based spectral-domain OCT device [23], with a low-coherence near-infrared light source (LS200B, Thorlabs, New Jersey, USA). This light source delivers 10 mW of optical power at a center wavelength of 1300 nm and bandwidth > 170 nm at the tip of a single-mode fiber. After passing through a transmission grating (1145 lines/mm, Wasatch Photonics, Utah, USA)

the interference patterns were projected on the sensor array of a 1024 pixel line CCD (LDH2, Goodrich, New Jersey, USA) to be recorded and transferred to a personal computer. This system uses single-mode fibers with nominal numerical aperture between 0.13 and 0.15 (SM980-5.8-125, Thorlabs, New Jersey, USA) and FC/APC connectors to deliver light to the sample and reference arms. At each arm a collimating lens with a focal length of 18.67 mm (F280APC-C, Thorlabs, New Jersey, USA) was used to collimate the output of the fiber. This lens provides a beam diameter of $3.4 \text{ mm} \times \frac{1}{\sqrt{2}}$ at 1310 nm when used with a single-mode fiber (SMF-28-J9, Thorlabs, New Jersey, USA). The OCT scanner utilizes a $10 \times$ telecentric objective lens with an effective focal length of 18 mm (LSM02, Thorlabs, New Jersey, USA).

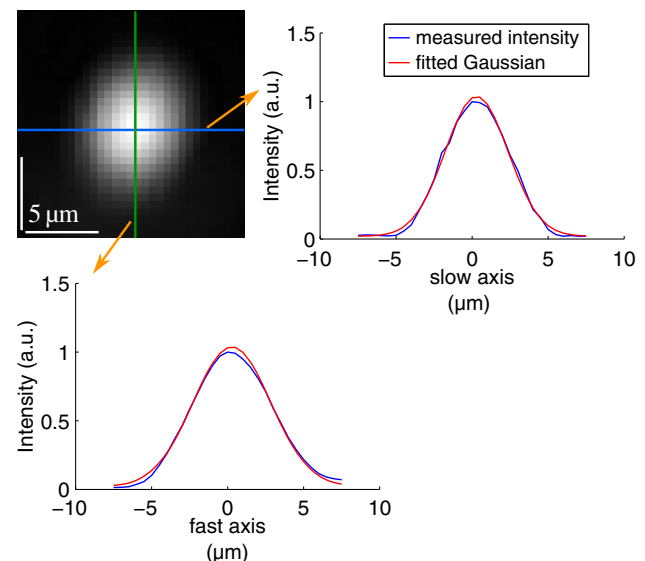


Fig. 8. Typical lateral PSF measured for semi-Plössl relay-lens system. A 2D Gaussian function is fitted to the PSF to measure the FWHM along the fast and slow scan-mirror axes. Cross sectional profile of the PSF and the fitted Gaussian function are plotted for each of the fast and slow axis directions.

To steer the light beam laterally on a sample, we used a two-axis galvanometric mirror system with a fast and slow rotating mirror (GVS002, Thorlabs, New Jersey, USA). The separation between mirrors was ~ 10 mm and the BFP of the scan lens was placed between the mirrors at the distance of 5 mm from each mirror.

C. Point-Spread Function Measurement

The prepared 3D sample was scanned by the custom-made OCT system. The scan parameters were set to cover a sub-area of $400 \mu\text{m} \times 400 \mu\text{m}$ on the phantom with $0.5 \mu\text{m}$ spacing between axial scans (A scans). Eight-hundred axial scans were recorded along the fast galvanometric mirror axis at the speed of 20,000 A scans per second to form a B scan. For each cross section, 10 B scans were recorded and averaged to reduce noise. The slow moving mirror was moved to the new cross section. This process was repeated for 800 different cross sections. The

data was further processed to detect and extract transversal images of gold nano-shells, which represent the lateral PSF of the imaging system at that sub-area. The FWHM of each PSF at the focal plane of the objective was measured and averaged to obtain the FWHM of the imaging system at that sub-area. To calculate the FWHM of a PSF, first a 2D Gaussian function was fitted [35] to the particle image. The FWHM along the fast (F) and slow (S) mirror directions were then calculated by $\text{FWHM}_{F/S} = 2\sqrt{2 \ln(2)}\sigma_{F/S}$ where σ_F and σ_S are the standard deviations of the fitted 2D Gaussian function along the fast and slow mirror axes, respectively (Fig. 8).

This procedure was repeated at different sub-areas across the entire FOV to obtain a map of the imaging resolution. Figure 9 presents the measured FWHM at different positions when achromatic doublets or four-element semi-Plössl lenses were used as the scan lens and tube lens. For the first-lens mechanism a $4 \text{ mm} \times 4 \text{ mm}$ area was scanned; however, due to the large PSF size and low signal to noise ratio at the borders of the FOV, the

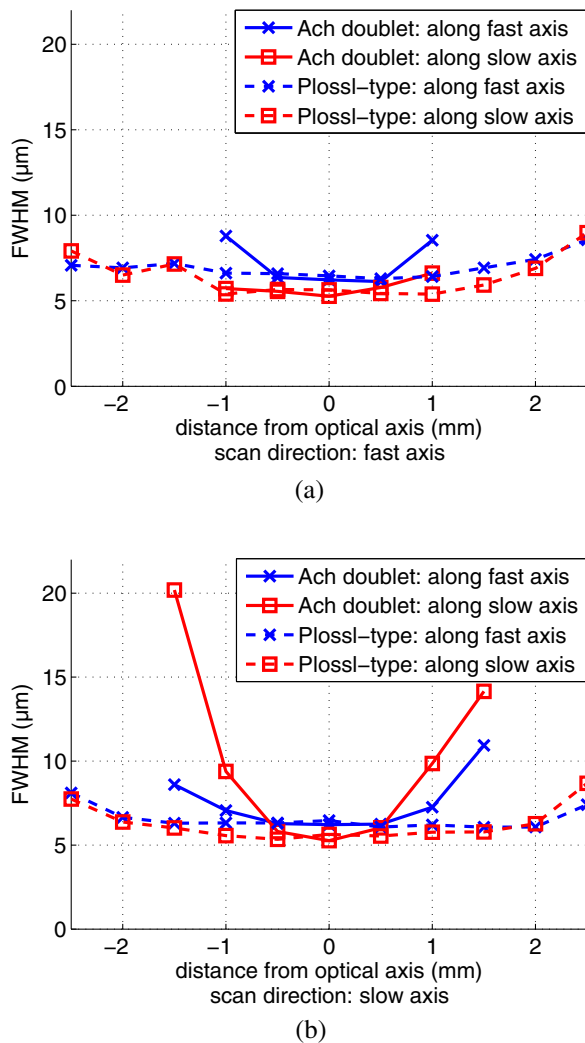


Fig. 9. FWHM of the PSF of the OCT system in the transversal plane at different positions (a) along the fast-mirror axis and (b) the slow mirror axis. FWHM of the lateral PSF of the OCT system with the semi-Plössl lens mechanism remains below $8 \mu\text{m}$ for positions up to 2 mm away from the center of FOV view. For the single achromatic doublet lens at the 1 mm distance from the optical axis FWHM exceeds $8 \mu\text{m}$.

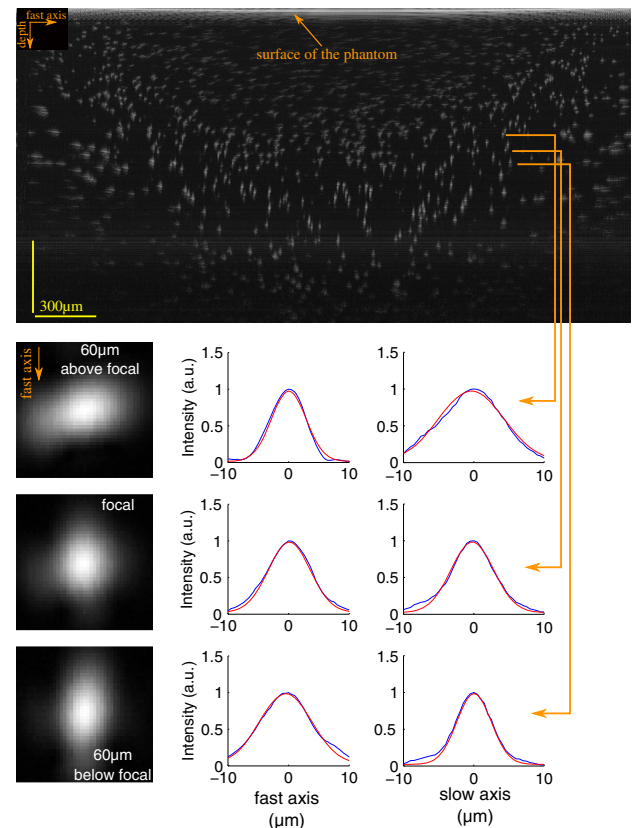


Fig. 10. Top: a 2D cross-sectional image taken when two achromatic doublets were used as the scan lens and tube lens. To be able to see out-of-focus particles a logarithmic scaling is used, which compresses the dynamic range of the image intensity. The out-of-focus nano-shell gold particles have much smaller intensity and the corresponding PSF is spread over a larger area compared to the particles in the focal of the objective lens. The field curvature is considerable and at the sides of the image the focal approaches toward the surface. Typical lateral PSF measurements at 1 mm from the center of FOV are shown at the lower panel. Due to astigmatism, PSF's are not similar above and below the focal surface. The arrows are just for illustrative purposes and are not showing the exact location of PSF measurements since they were obtained from a different recording.

resolution measurements were performed only at the central 2 mm × 2 mm area. With this lens mechanism at 1 mm away from the optical axis, the FWHM increased to ~8 and ~10 μm along the fast and slow axes, respectively. Therefore, the maximum FOV with close to the diffraction-limited resolution that our OCT system could achieve with this lens systems was ~2 mm in diameter. Another important imperfection caused by the first relay lens was the large field curvature. Because of astigmatism, the curvature was different for tangential and sagittal rays. Tangential focal curvature can be observed in a cross-sectional image captured from the 3D phantom (Fig. 10) in which the out-of-focus particles become larger and their intensity drops. For the lens system that consists of four-element semi-Plössl compounds, the resolution is 5.6 and 6.4 μm at the center of FOV along the fast and slow axes, respectively, and remains fairly uniform across most of the FOV. At scan angles larger than 6.4°, the FWHM increases above 7 μm along both axes, possibly due to aberrations or beam cut at the edge of the lenses.

4. CONCLUSION

Optical aberrations associated with three popular and economical scan-/tube-lens systems were analyzed and the performance of two of these lens mechanisms was experimentally measured in an OCT scanner. Our simulations demonstrated that using singlet lenses or achromatic doublets as a scan/tube lens reduces the FOV with diffraction-limited resolution and degrades the quality of OCT images due to astigmatism and field curvature. A four-element semi-Plössl compound lens system provides superior performance over an FOV of diameter 4 mm when used in combination with an objective of focal length 18 mm. To experimentally measure the resolution of OCT systems with different scan-/tube-lens mechanisms, we prepared a transparent 3D phantom with embedded gold nano-shells. The outer diameter of these particles was ~231 nm, which was significantly smaller than the theoretical resolution of our OCT system. Using this 3D phantom, the PSF of the OCT system for each of the scan-/tube-lens mechanisms was measured experimentally. These measurements confirm that an achromatic doublet lens as a scan/tube lens cannot provide the diffraction-limited performance over a field of view larger than 2 mm in diameter; however, with the four-element semi-Plössl lens we were able to achieve PSF with the FWHM smaller than 7 μm over a FOV with a diameter of 4 mm. This performance is acceptable for many OCT applications; however, to achieve a larger FOV, custom-made Plössl lenses similar to what has been presented in [24] can be employed. In fiber-based OCT scanners, backscattered photons need to couple back into the same single-mode optical fiber from which they are emitted; therefore, light travels back and forth through the same optical components. A comprehensive two-way simulation is necessary to analyze aberrations in a more accurate manner and also to consider diffraction effects on the overall resolution. The authors also suggest investigating the far-field backscattering by the gold nano-shells under Gaussian field illumination. This can give a better insight on possible differences between the measured resolution with a gold nano-shell phantom and real-word specimens.

Funding. Research Growth Initiative (RGI), University of Wisconsin (101X213/101X254); NARSAD (20610); National Science Foundation (NSF) (1454300).

Acknowledgment. The authors thank Professor Rohatgi and Afsaneh Dorri at the UWM Center for Composites for their help and support in preparing the 3D gold nano-shell phantom.

REFERENCES

1. D. Huang, E. A. Swanson, C. P. Lin, J. S. Schuman, W. G. Stinson, W. Chang, M. R. Hee, T. Flotte, K. Gregory, C. A. Puliafito, and J. G. Fujimoto, "Optical coherence tomography," *Science* **254**, 1178–1181 (1991).
2. J. G. Fujimoto, "Optical coherence tomography for ultrahigh resolution in vivo imaging," *Nat. Biotechnol.* **21**, 1361–1367 (2003).
3. B. White, M. Pierce, N. Nassif, B. Cense, B. Park, G. Tearney, B. Bouma, T. Chen, and J. F. de Boer, "In vivo dynamic human retinal blood flow imaging using ultra-high-speed spectral domain optical coherence tomography," *Opt. Express* **11**, 3490–3497 (2003).
4. S. H. Yun, G. J. Tearney, B. E. Bouma, B. H. Park, and J. F. de Boer, "High-speed spectral-domain optical coherence tomography at 1.3 μm wavelength," *Opt. Express* **11**, 3598–3604 (2003).
5. N. A. Nassif, B. Cense, B. H. Park, M. C. Pierce, S. H. Yun, B. E. Bouma, G. J. Tearney, T. C. Chen, and J. F. de Boer, "In vivo high-resolution video-rate spectral-domain optical coherence tomography of the human retina and optic nerve," *Opt. Express* **12**, 367–376 (2004).
6. V. J. Srinivasan, E. T. Mandeville, A. Can, F. Blasi, M. Klimov, A. Daneshmand, J. H. Lee, E. Yu, H. Radhakrishnan, E. H. Lo, S. Sakadzic, K. Eikermann-Haerter, and C. Ayata, "Multiparametric, longitudinal optical coherence tomography imaging reveals acute injury and chronic recovery in experimental ischemic stroke," *PLoS One* **8**, e71478 (2013).
7. R. Zawadzki, S. Jones, S. Olivier, M. Zhao, B. Bower, J. Izatt, S. Choi, S. Laut, and J. Werner, "Adaptive-optics optical coherence tomography for high-resolution and high-speed 3D retinal in vivo imaging," *Opt. Express* **13**, 8532–8546 (2005).
8. M. Szkulmowski, A. Szkulmowska, T. Bajraszewski, A. Kowalczyk, and M. Wojtkowski, "Flow velocity estimation using joint spectral and time domain optical coherence tomography," *Opt. Express* **16**, 6008–6025 (2008).
9. D. Y. Kim, J. Fingler, J. S. Werner, D. M. Schwartz, S. E. Fraser, and R. J. Zawadzki, "In vivo volumetric imaging of human retinal circulation with phase-variance optical coherence tomography," *Biomed. Opt. Express* **2**, 1504–1513 (2011).
10. B. J. Vakoc, R. M. Lanning, J. A. Tyrrell, T. P. Padera, L. A. Bartlett, T. Stylianopoulos, L. L. Munn, G. J. Tearney, D. Fukumura, R. K. Jain, and B. E. Bouma, "Three-dimensional microscopy of the tumor microenvironment in vivo using optical frequency domain imaging," *Nat. Med.* **15**, 1219–1223 (2009).
11. J. Qin, L. Shi, H. Wang, R. Reif, and R. K. Wang, "Functional evaluation of hemodynamic response during neural activation using optical microangiography integrated with dual-wavelength laser speckle imaging," *J. Biomed. Opt.* **19**, 026013 (2014).
12. W. Choi, B. Potsaid, V. Jayaraman, B. Baumann, I. Grulkowski, J. J. Liu, C. D. Lu, A. E. Cable, D. Huang, J. S. Duker, and J. G. Fujimoto, "Phase-sensitive swept-source optical coherence tomography imaging of the human retina with a vertical cavity surface-emitting laser light source," *Opt. Lett.* **38**, 338–340 (2013).
13. K. Beaudette, H. W. Baac, W.-J. Madore, M. Villiger, N. Godbout, B. E. Bouma, and C. Boudoux, "Laser tissue coagulation and concurrent optical coherence tomography through a double-clad fiber coupler," *Biomed. Opt. Express* **6**, 1293–1303 (2015).
14. B. Povazay, K. Bizheva, A. Unterhuber, B. Hermann, H. Sattmann, A. F. Fercher, W. Drexler, A. Apolonski, W. J. Wadsworth, J. C. Knight, P. St.J. Russell, M. Vetterlein, and E. Scherzer,

- "Submicrometer axial resolution optical coherence tomography," *Opt. Lett.* **27**, 1800–1802 (2002).
15. A. Dubois, G. Moneron, K. Grieve, and A. C. Boccara, "Three-dimensional cellular-level imaging using full-field optical coherence tomography," *Phys. Med. Biol.* **49**, 1227–1234 (2004).
 16. G. Humbert, W. J. Wadsworth, S. G. Leon-Saval, J. C. Knight, T. A. Birks, P. St.J. Russell, M. J. Lederer, D. Kopf, K. Wiesauer, E. I. Breuer, and D. Stifter, "Supercontinuum generation system for optical coherence tomography based on tapered photonic crystal fibre," *Opt. Express* **14**, 1596–1603 (2006).
 17. D. Sacchet, J. Moreau, P. Georges, and A. Dubois, "Simultaneous dual-band ultra-high resolution full-field optical coherence tomography," *Opt. Express* **16**, 19434–19446 (2008).
 18. L. Liu, J. A. Gardecki, S. K. Nadkarni, J. D. Toussaint, Y. Yagi, B. E. Bouma, and G. J. Tearney, "Imaging the subcellular structure of human coronary atherosclerosis using micro-optical coherence tomography," *Nat. Med.* **17**, 1010–1014 (2011).
 19. P. Steiner, V. Enzmann, C. Meier, B. Povazay, and J. H. Kowal, "Retinal laser lesion visibility in simultaneous ultra-high axial resolution optical coherence tomography," *IEEE Photon. J.* **6**, 1–11 (2014).
 20. B. Jeong, B. Lee, M. S. Jang, H. Nam, S. J. Yoon, T. Wang, J. Doh, B.-G. Yang, M. H. Jang, and K. H. Kim, "Combined two-photon microscopy and optical coherence tomography using individually optimized sources," *Opt. Express* **19**, 13089–13096 (2011).
 21. T. Wang, J. J. Mancuso, S. M. Shams Kazmi, J. Dwelle, V. Sapozhnikova, B. Willsey, L. L. Ma, J. Qiu, X. Li, A. K. Dunn, K. P. Johnston, M. D. Feldman, and T. E. Milner, "Combined two-photon luminescence microscopy and OCT for macrophage detection in the hypercholesterolemic rabbit aorta using plasmonic gold nanorose," *Lasers Surg. Med.* **44**, 49–59 (2012).
 22. T. Wang, Q. Li, P. Xiao, J. Ahn, Y. E. Kim, Y. Park, M. Kim, M. Song, E. Chung, W. K. Chung, G.-O. Ahn, S. Kim, P. Kim, S.-J. Myung, and K. H. Kim, "Gradient index lens based combined two-photon microscopy and optical coherence tomography," *Opt. Express* **22**, 12962–12970 (2014).
 23. F. Atry, S. Frye, T. J. Richner, S. K. Brodnick, A. Soehartono, J. Williams, and R. Pashaie, "Monitoring cerebral hemodynamics following optogenetic stimulation via optical coherence tomography," *IEEE Trans. Biomed. Eng.* **62**, 766–773 (2015).
 24. A. Negrean and H. D. Mansvelder, "Optimal lens design and use in laser-scanning microscopy," *Biomed. Opt. Express* **5**, 1588–1609 (2014).
 25. S. Meissner, L. Knels, A. Krueger, T. Koch, and E. Koch, "Simultaneous three-dimensional optical coherence tomography and intravital microscopy for imaging subpleural pulmonary alveoli in isolated rabbit lungs," *J. Biomed. Opt.* **14**, 054020 (2009).
 26. L. Shi, J. Qin, R. Reif, and R. K. Wang, "Wide velocity range Doppler optical microangiography using optimized step-scanning protocol with phase variance mask," *J. Biomed. Opt.* **18**, 106015 (2013).
 27. B. J. Vakoc, D. Fukumura, R. K. Jain, and B. E. Bouma, "Cancer imaging by optical coherence tomography: preclinical progress and clinical potential," *Nat. Rev. Cancer* **12**, 363–368 (2012).
 28. P. M. Andrews, Y. Chen, M. L. Onozato, S.-W. Huang, D. C. Adler, R. A. Huber, J. Jiang, S. E. Barry, A. E. Cable, and J. G. Fujimoto, "High-resolution optical coherence tomography imaging of the living kidney," *Lab. Invest.* **88**, 441–449 (2008).
 29. J. Lee, H. Radhakrishnan, W. Wu, A. Daneshmand, M. Klimov, C. Ayata, and D. A. Boas, "Quantitative imaging of cerebral blood flow velocity and intracellular motility using dynamic light scattering-optical coherence tomography," *J. Cereb. Blood Flow Metab.* **33**, 819–825 (2013).
 30. E. A. B. Saleh and M. C. Teich, "Beam Optics," in *Fundamentals of Photonics* (Wiley, 2007), pp. 74–101.
 31. P. D. Woolliams and P. H. Tomlins, "Estimating the resolution of a commercial optical coherence tomography system with limited spatial sampling," *Meas. Sci. Technol.* **22**, 065502 (2011).
 32. A. Fouad, T. Joshua Pfefer, C.-W. Chen, W. Gong, A. Agrawal, P. H. Tomlins, P. D. Woolliams, R. A. Drezek, and Y. Chen, "Variations in optical coherence tomography resolution and uniformity: a multi-system performance comparison," *Biomed. Opt. Express* **5**, 2066–2081 (2014).
 33. M. Avanaki, A. G. Podoleanu, M. C. Price, S. A. Corr, and S. A. Hojjatoleslami, "Two applications of solid phantoms in performance assessment of optical coherence tomography systems," *Appl. Opt.* **52**, 7054–7061 (2013).
 34. A. Agrawal, T. J. Pfefer, N. Gilani, and R. Drezek, "Three-dimensional characterization of optical coherence tomography point spread functions with a nanoparticle-embedded phantom," *Opt. Lett.* **35**, 2269–2271 (2010).
 35. G. Nootz, "Fit 2D Gaussian function to data," 2012, <http://www.mathworks.com/matlabcentral/fileexchange/37087> [Retrieved Nov. 11 2014].